# Supplementary Materials for

## Fragmented Liquid Crystals of Graphene Oxide

Chenwei Shen, Yangchao Liao *et al.*

*Corresponding author. Email: zhenxu@zju.edu.cn (Zhen Xu); xuzp@tsinghua.edu.cn (Zhiping Xu)

**This PDF file includes:**

## 1. Figures S1 to S30

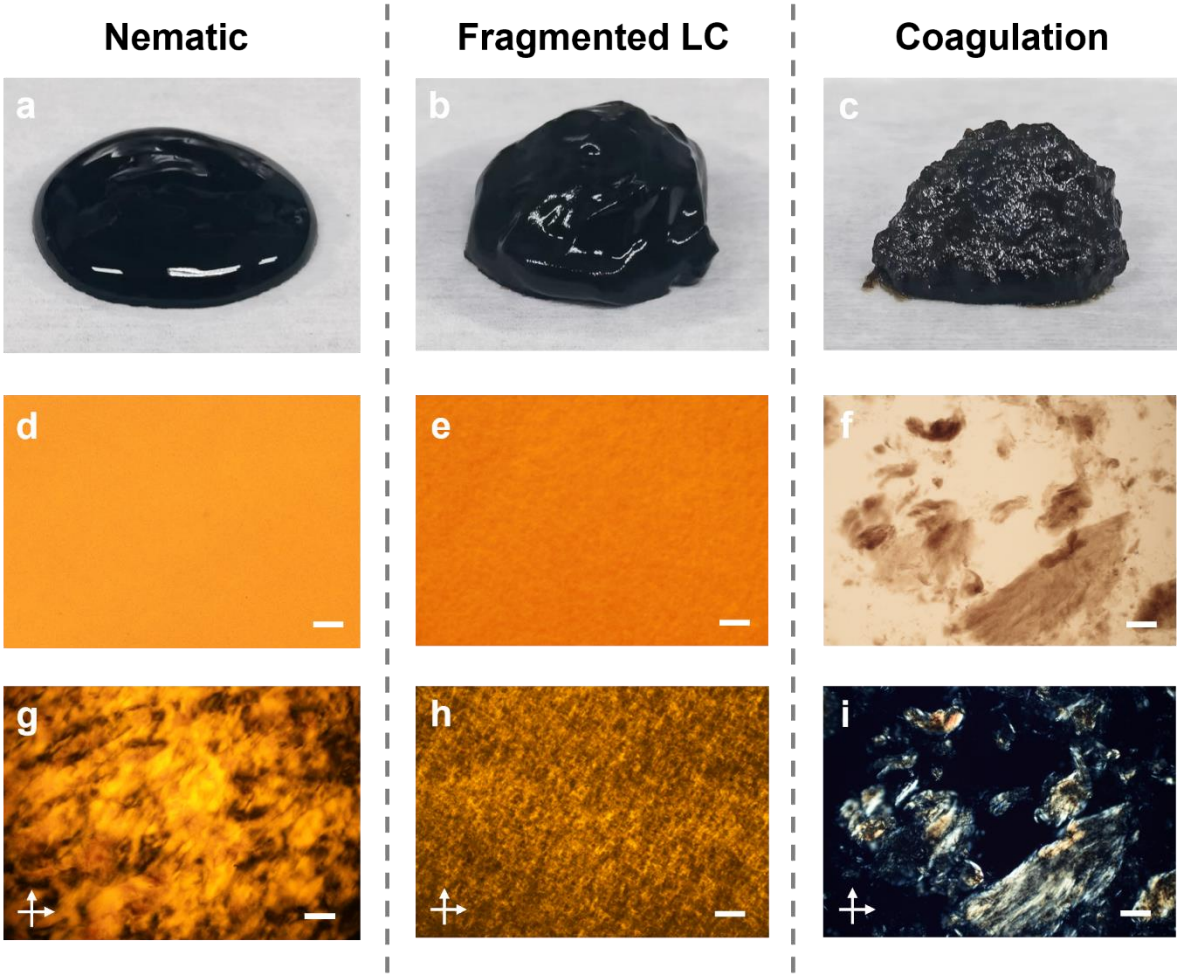


**Fig. S1. Basic characteristics of GO dispersions in different states.** The Photographs **(a-c)**, OM images **(d-f)** and POM images **(g-i)** of nematic LC state, FLC state and coagulation state. Scale bars: 200 μm **(d-i)**.

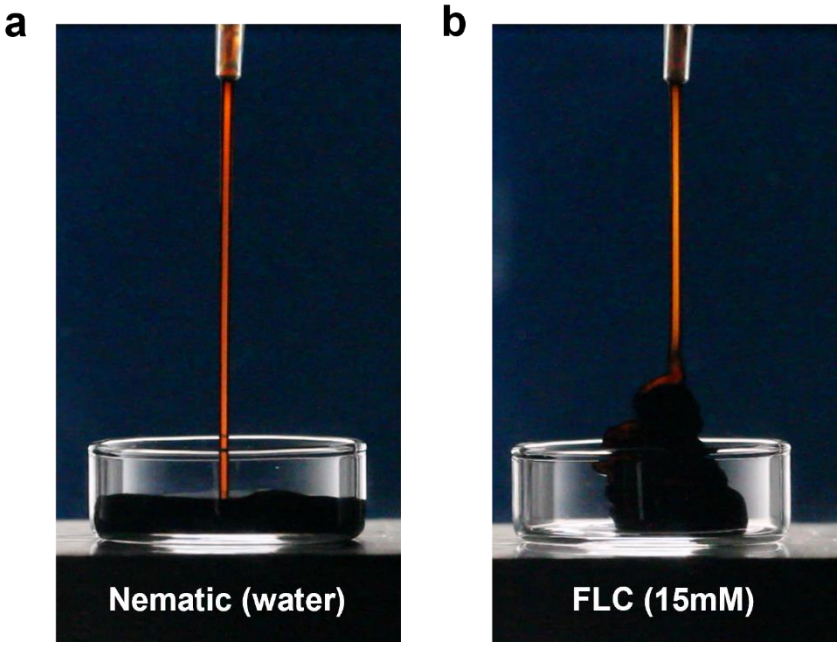


**Fig. S2. Flowing GO dispersion between crossed polarizers in nematic LC and FLC state.**

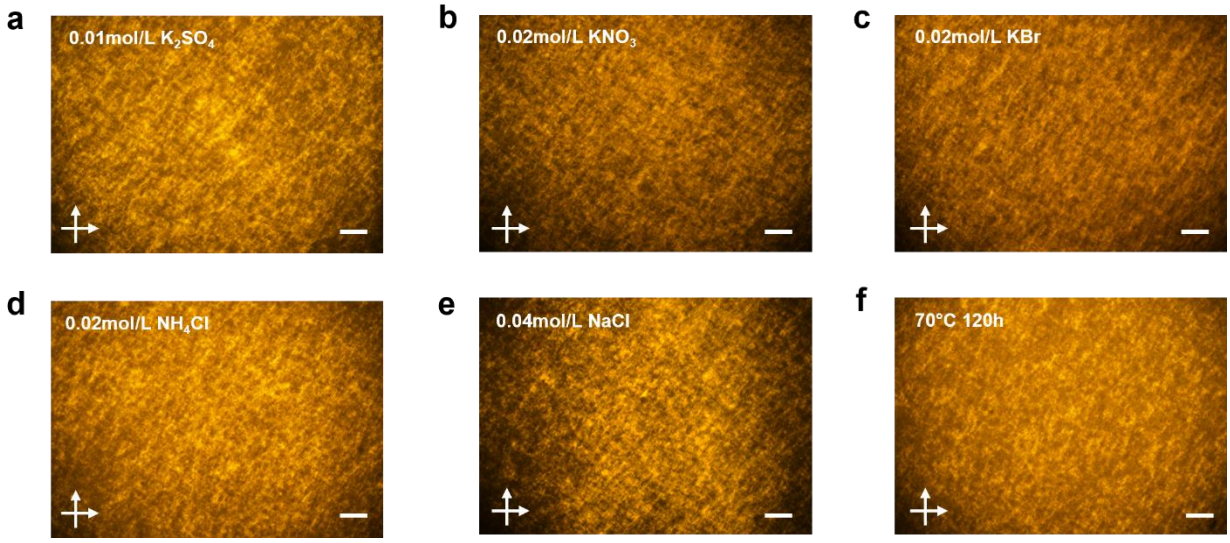


**Fig. S3. The generality of FLCs.** POM images of GOFLCs induced by the addition of $K_2SO_4$ (**a**), $KNO_3$ (**b**), KBr (**c**), $NH_4Cl$ (**d**), NaCl (**e**) and moderate heating (**f**). The concentration of salt in 10mg/g GO is shown on the upper left corner of the picture. Scale bars: 200 μm (**a-f**).

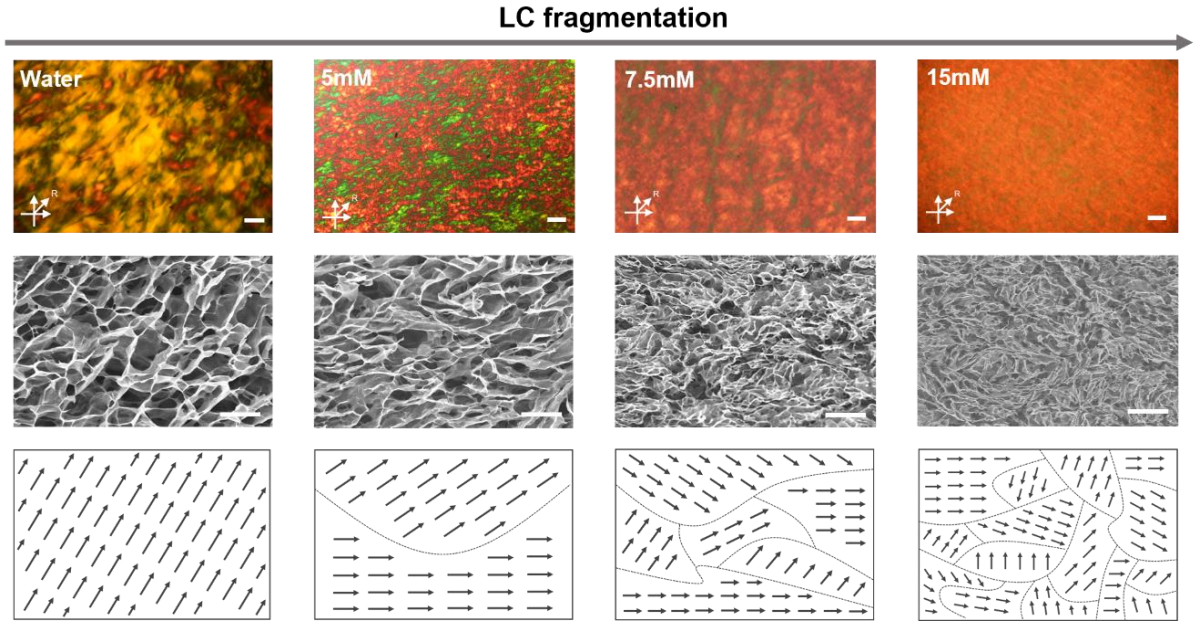


**Fig. S4. Tracking of the LC fragmentation process.** POM images with retardation plate (the upper row) and cross-sectional SEM images (the middle row) of freeze-dried GO dispersions are used to track the LC fragmentation process with increasing KCl concentrations by. The GO sheets orientation in corresponding SEM images are also presented (the bottom row). Scale bars: 200 μm (the upper row), 20 μm (the middle row).

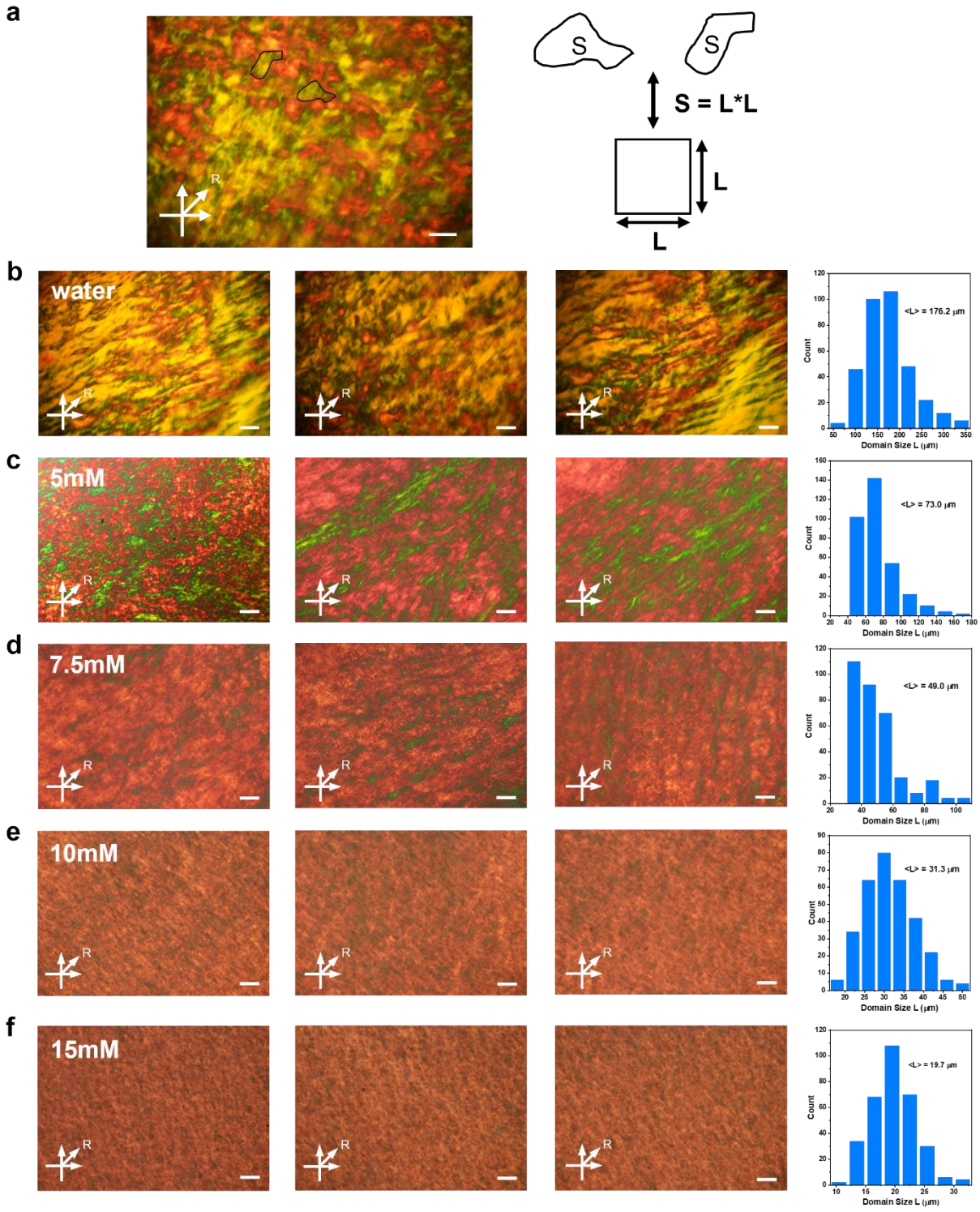
a
S
S
S = L*L
L
L
R
b
water
<L> = 176.2 μm
Count
Domain Size L (μm)
c
5mM
<L> = 73.0 μm
Count
Domain Size L (μm)
d
7.5mM
<L> = 49.0 μm
Count
Domain Size L (μm)
e
10mM
<L> = 31.3 μm
Count
Domain Size L (μm)
f
15mM
<L> = 19.7 μm
Count
Domain Size L (μm)

**Fig. S5. The LC fragmentation process of GO dispersion with increasing KCl concentrations.** **a** The statistical method of the size of LC regions. **b-f** POM images with retardation plate and the statistical results of the size of LC regions of pure GO dispersion **(b)** and GO dispersion with the addition of 5mM **(c)**, 7.5mM **(d)**, 10mM **(e)** and 15mM **(f)** KCl. Scale bars: 200 μm **(b-f)**.

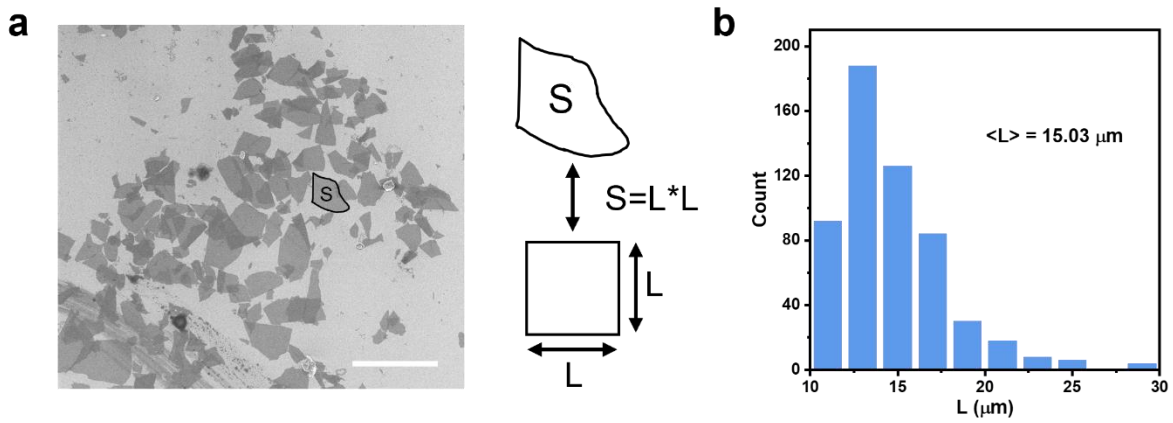


**Fig. S6. statistical method and statistical results of the size of GO sheets.** Scale bars: 40 μm.

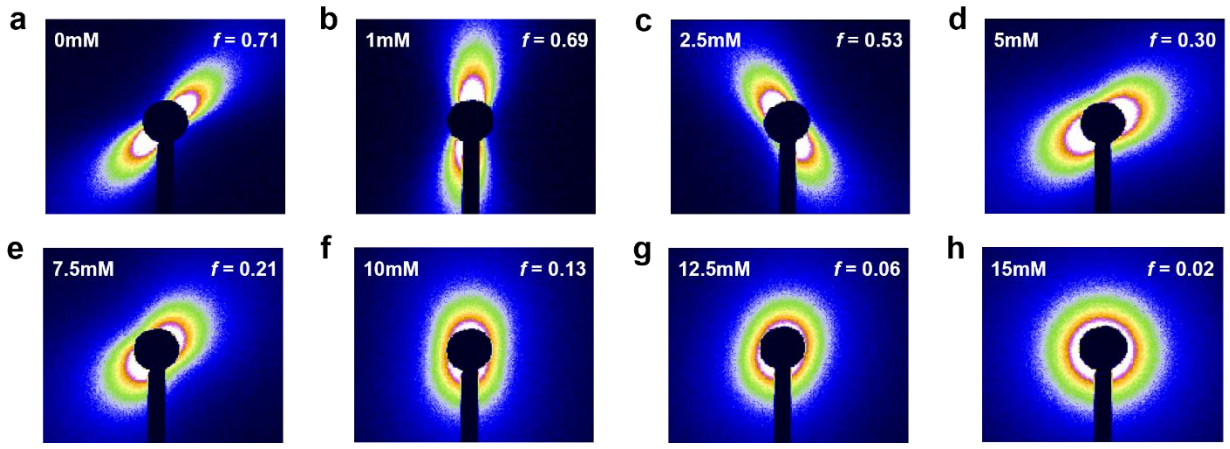


**Fig. S7. The evolution of SAXS patterns of GO dispersions with increasing KCl concentration**

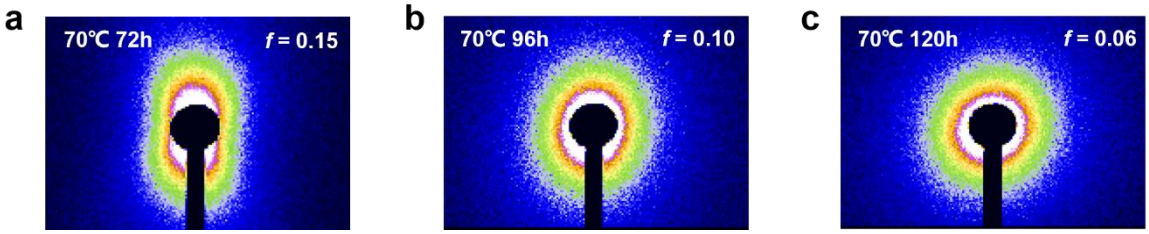


**Fig. S8. The evolution of SAXS patterns of GO dispersions with increasing heating time.**

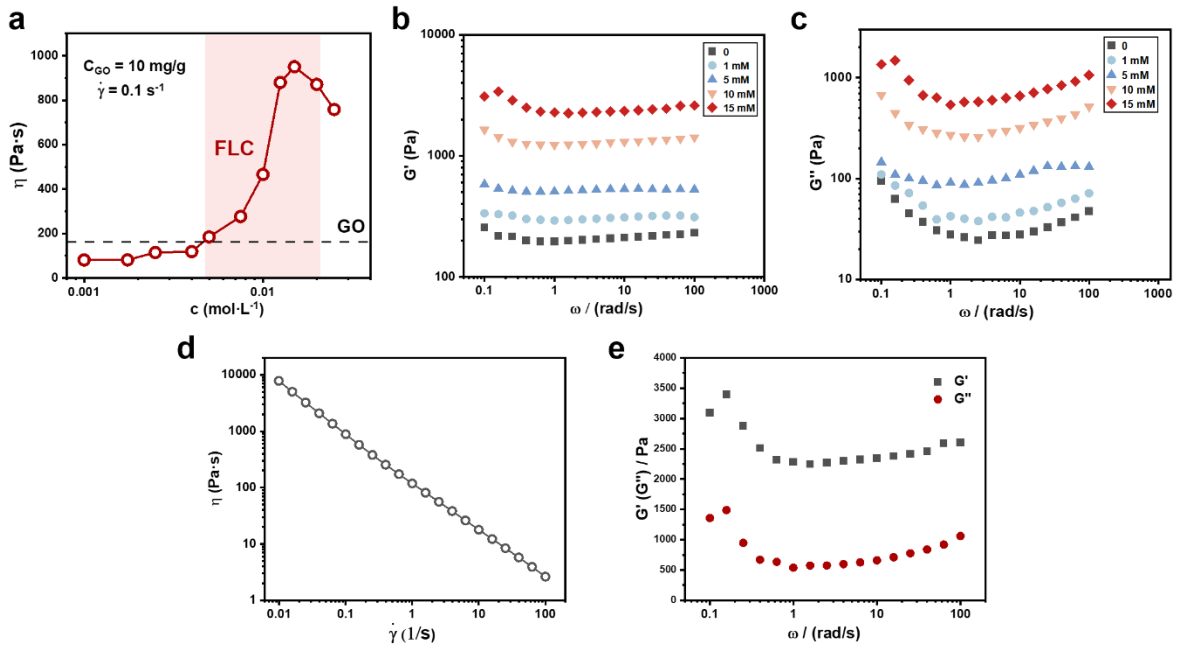


**Fig. S9. Rheological behaviors of GOFLCs. a** The effect of KCl addition on the viscosity of GO dispersion. The concentration of GO dispersions is 10 mg/g and the shear rate is 0.1 $s^{-1}$. **b, c** The storage moduli **(b)** and loss moduli **(c)** measured from the dynamic frequency sweeps of 10 $mg \cdot g^{-1}$ GO dispersion with the different KCl addition. **d, e** The shear thinning behavior **(d)** and typical oscillatory shear curves **(e)** of GOFLCs. The GOFLC dispersion is made by adding 15mM KCl to 10$mg \cdot g^{-1}$ GO dispersion.

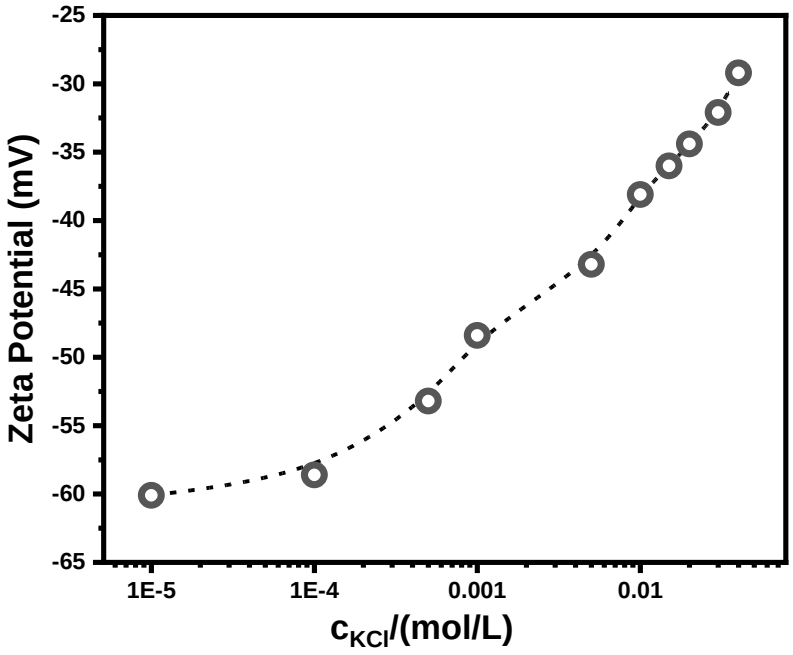


**Fig. S10. Zeta potential of the GO-KCl system as a function of KCl concentrations.**

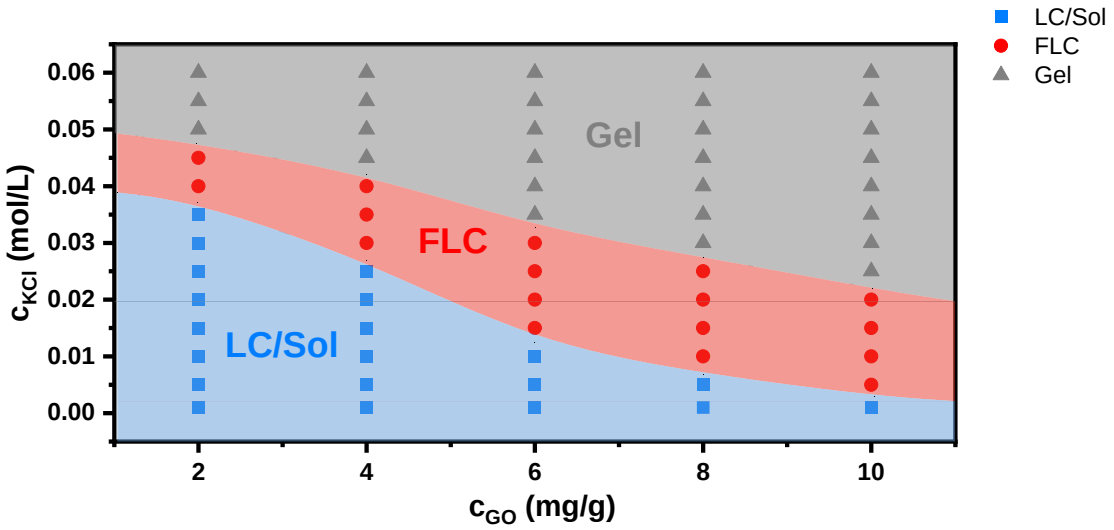


**Fig. S11. The experimental phase diagram of GO-KCl system.**

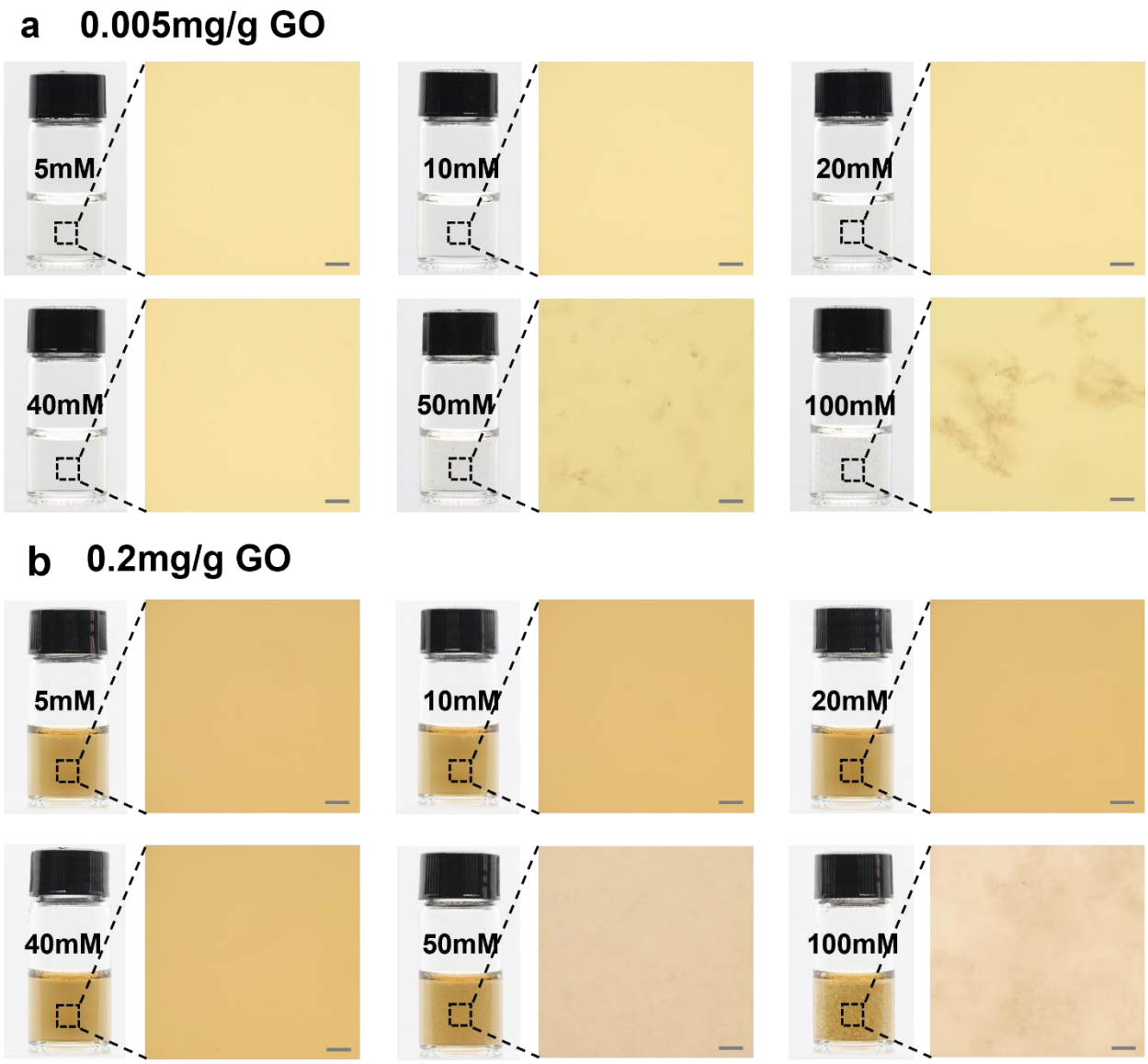


**Fig. S12. The dispersed state of GO sheets.** Photographs and OM images of 0.005mg/g **(a)** and 0.2mg/g **(b)** GO dispersion with different KCl concentrations. Scale bars: 100 μm.

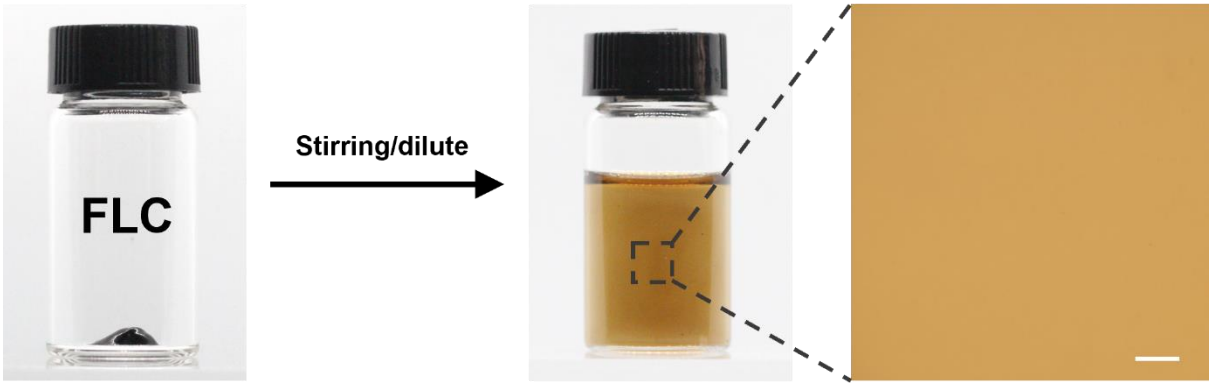


**Fig. S13. Dilution of GOFLCs and OM image of diluted GO dispersion.** Scale bars: 100 μm.

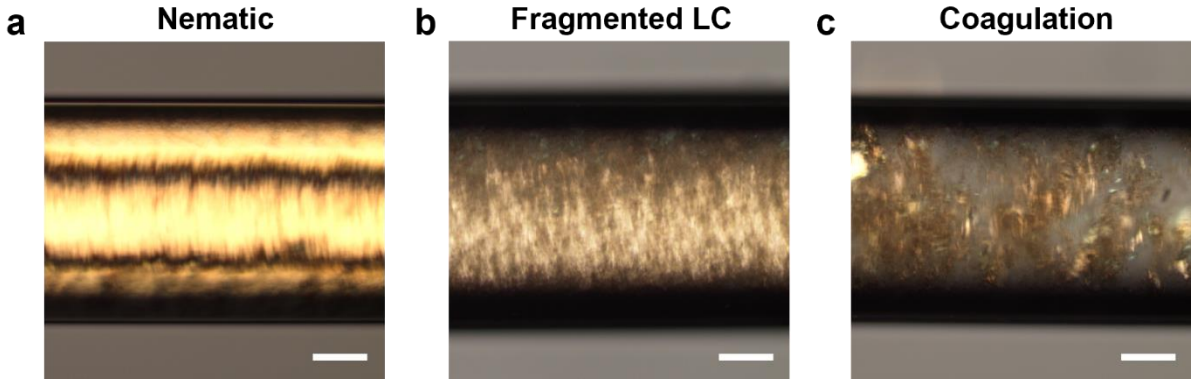


**Fig. S14. Flowing-induced LC director orientation.** POM images of GO dispersion at different states squeezed into capillaries. Scale bars: 100 μm.

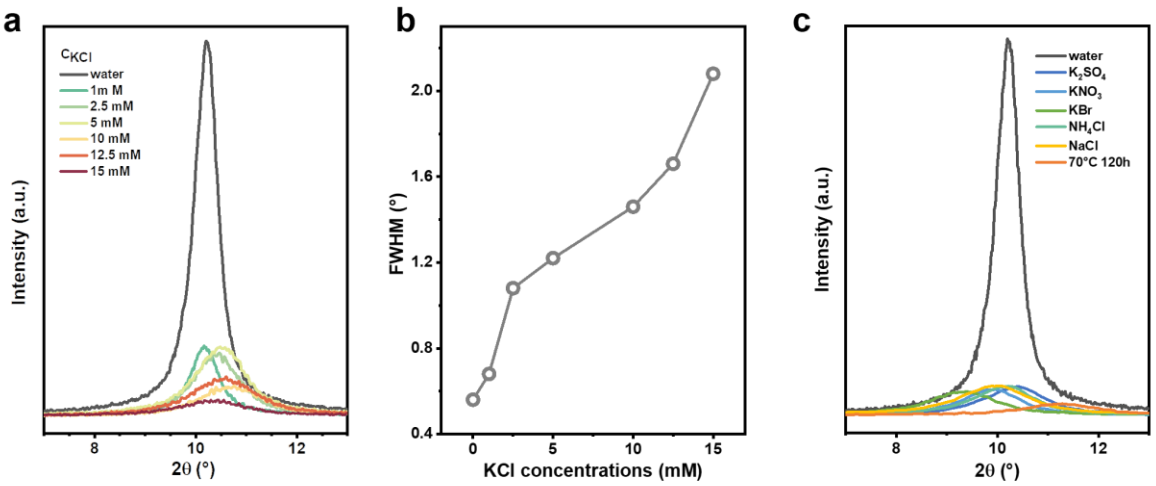


**Fig. S15. The decrystallization process of GO papers.** XRD patterns of GO papers with different KCl addition **(a)** and amorphous GO papers assembled from GOFLCs formed by other methods **(c)** and FWHM of diffraction peaks in a, showing gradual increase with increasing $C_{KCl}$ **(b)**.

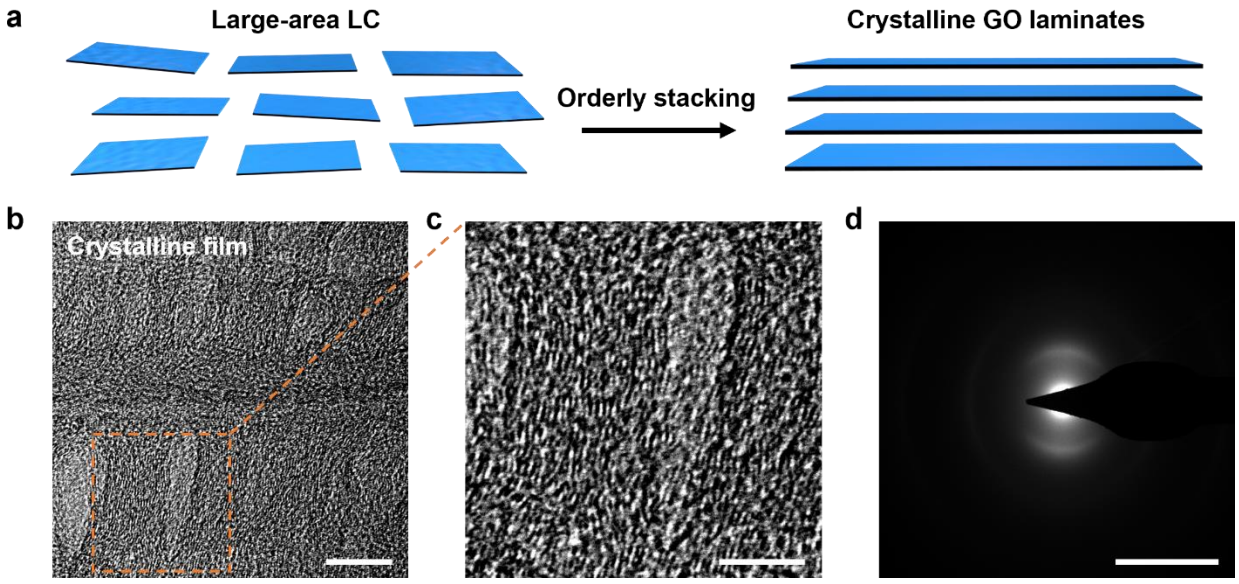


**Fig. S16. The crystalline structure of ordinary GO papers. a** Schematic illustration of the formation of GO crystals from large-area LCs. **b-d** High-resolution TEM images **(b, c)** and selected area electron diffraction **(d)** of crystalline GO papers made by pure GO dispersion with large-area LCs. Scale bars: 10 nm **(b)**, 5 nm **(c)**, 5 $nm^{-1}$ **(d)**.

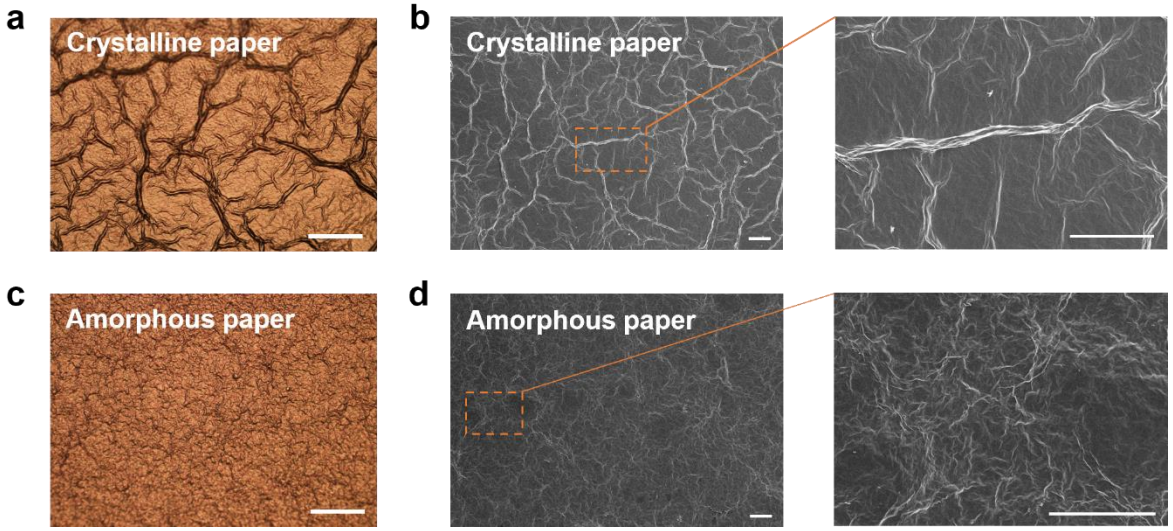


**Fig. S17. The surface morphology of GO papers. OM images (a, c) and SEM images (b, d) of the surface of crystalline GO papers and amorphous GO papers.** Scale bars: 100 μm **(a, c)**; 40μm **(b, d)**.

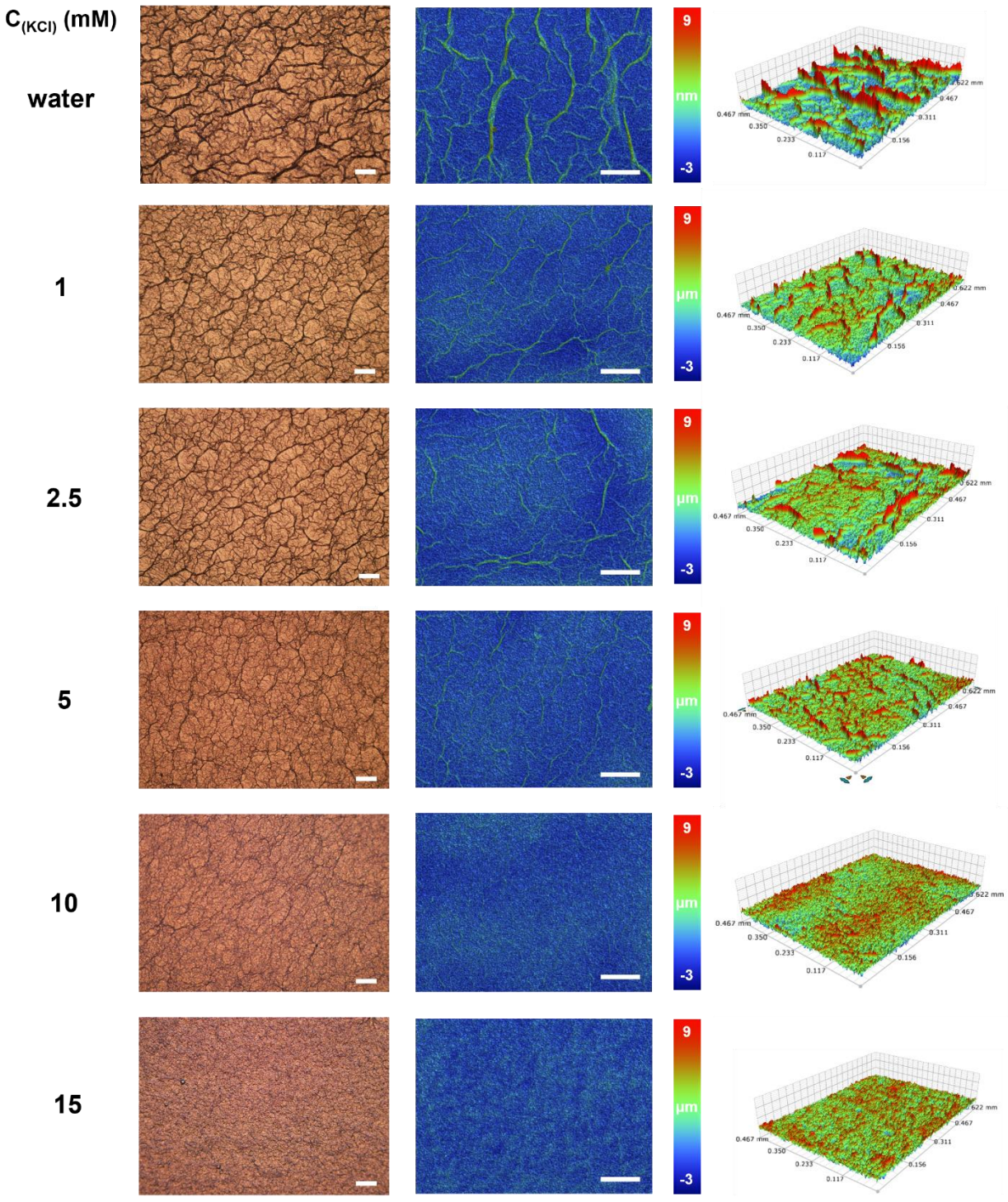
C(KCl) (mM)
water
1
2.5
5
10
15
9
nm
µm
-3
0.622 mm
0.467
0.311
0.156
0.467 mm
0.350
0.233
0.117

**Fig. S18. Evolution of GO paper surface morphology with increasing $C_{KCl}$.** The OM images, two-dimensional and three-dimensional white light interference microscopy images of blade casting papers made from 10mg/g GO dispersion with different $C_{KCl}$. Scale bars: 100 μm.

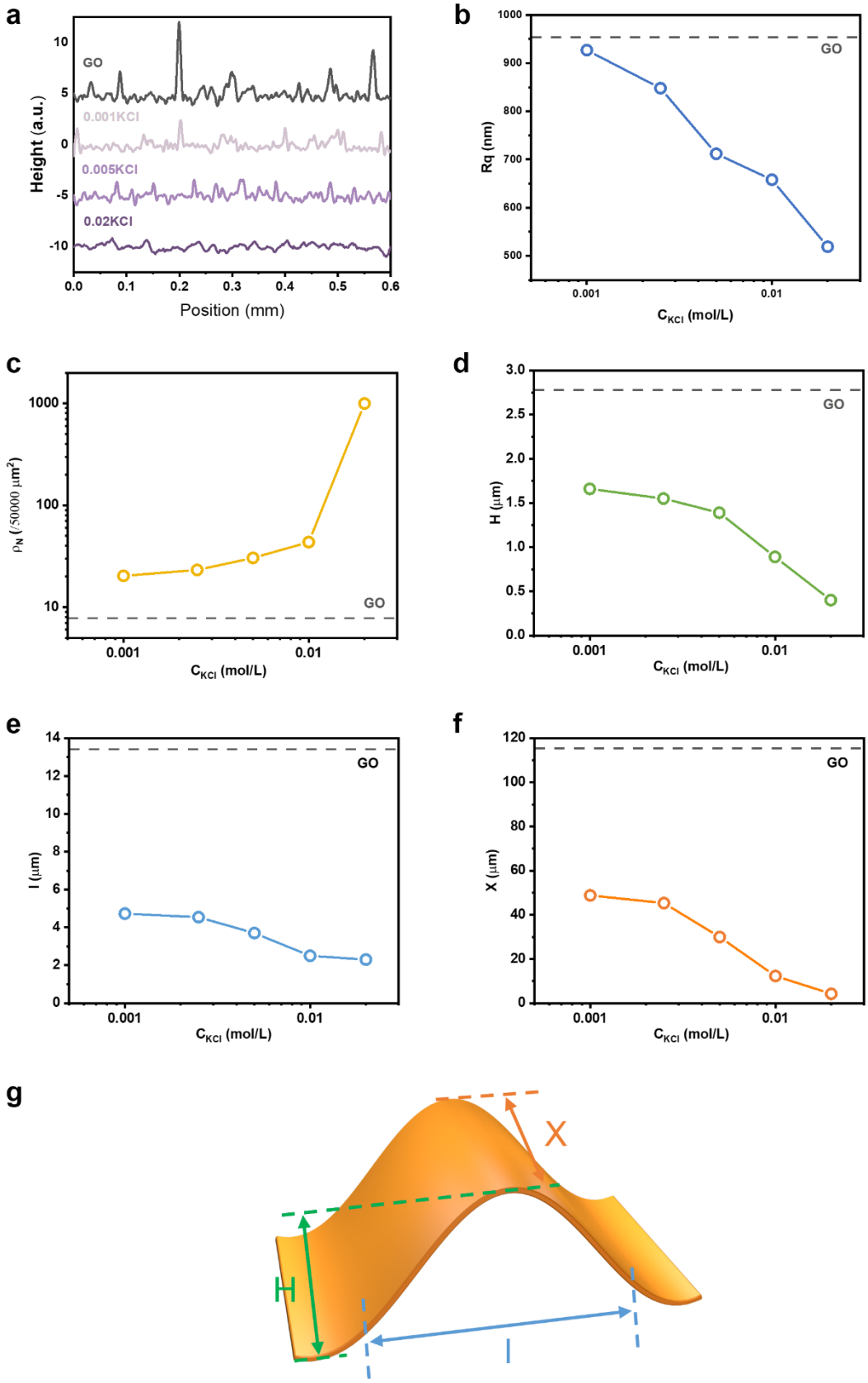
a
Height (a.u.)
Position (mm)
GO
0.001KCl
0.005KCl
0.02KCl
b
Rq (nm)
GO
$C_{KCl}$ (mol/L)
c
$\rho_N$ (/50000 μm²)
GO
$C_{KCl}$ (mol/L)
d
H (μm)
GO
$C_{KCl}$ (mol/L)
e
l (μm)
GO
$C_{KCl}$ (mol/L)
f
X (μm)
GO
$C_{KCl}$ (mol/L)
g
X
H
l

**Fig. S19. Evolution of the wrinkle characteristics with increasing $C_{KCl}$. a** Typical height profiles of papers made from GO dispersion with different $C_{KCl}$. **b-f** Plots of surface roughness **(b)**, wrinkle density **(c)**, wrinkle height **(d)**, wrinkle span **(e)** and wrinkle length **(f)** versus $C_{KCl}$. **(g)** Schematic illustration of the geometric parameters describing wrinkles.

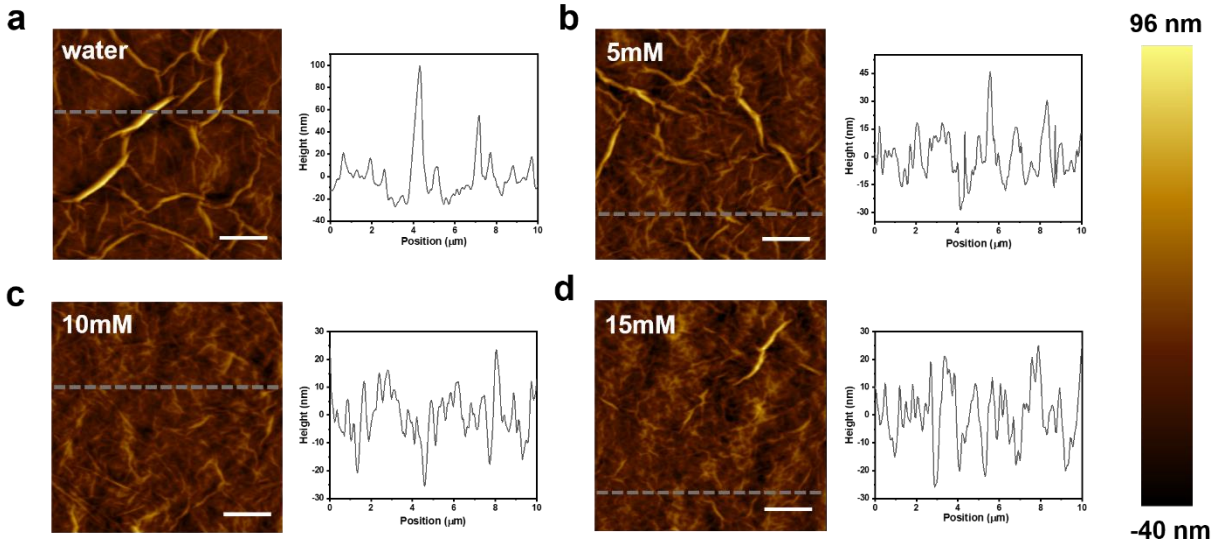


**Fig. S20. The surface morphology within single GO sheet.** AFM images and typical height profiles of GO papers with different KCl addition. Scale bars: 2 μm.

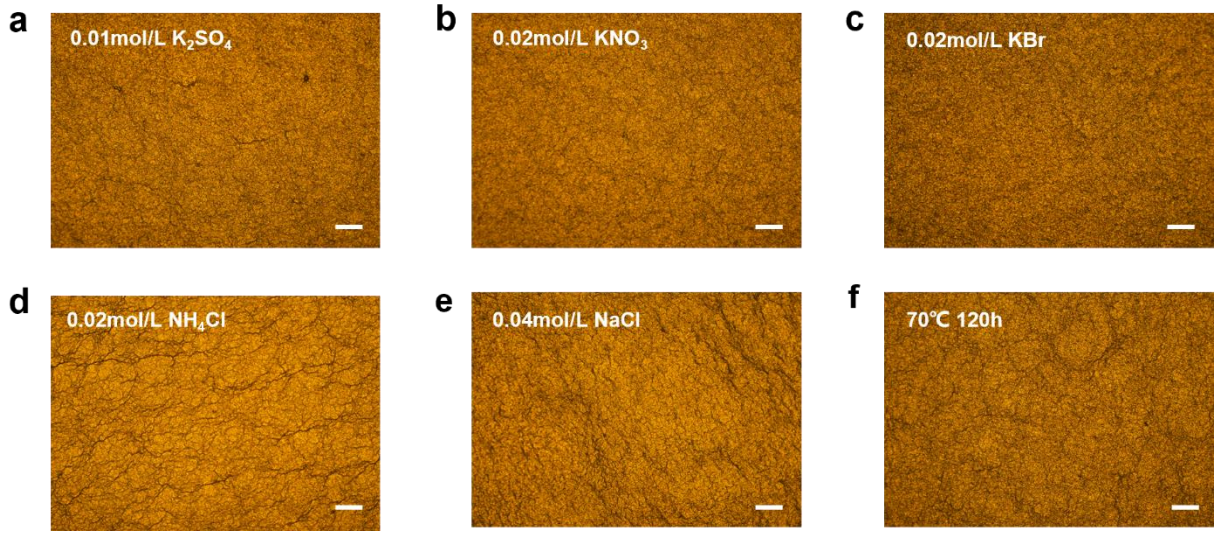


**Fig. S21. The surface morphology of other GOFLC amorphous papers.** OM images of amorphous GO papers assembled from GOFLCs formed by the addition of $K_2SO_4$ **(a)**, $KNO_3$ **(b)**, KBr **(c)**, $NH_4Cl$ **(d)**, NaCl **(e)** and moderate heating **(f)**. The concentration of salt in 10mg/g GO is shown on the upper left corner of the picture. Scale bars: 100 μm.

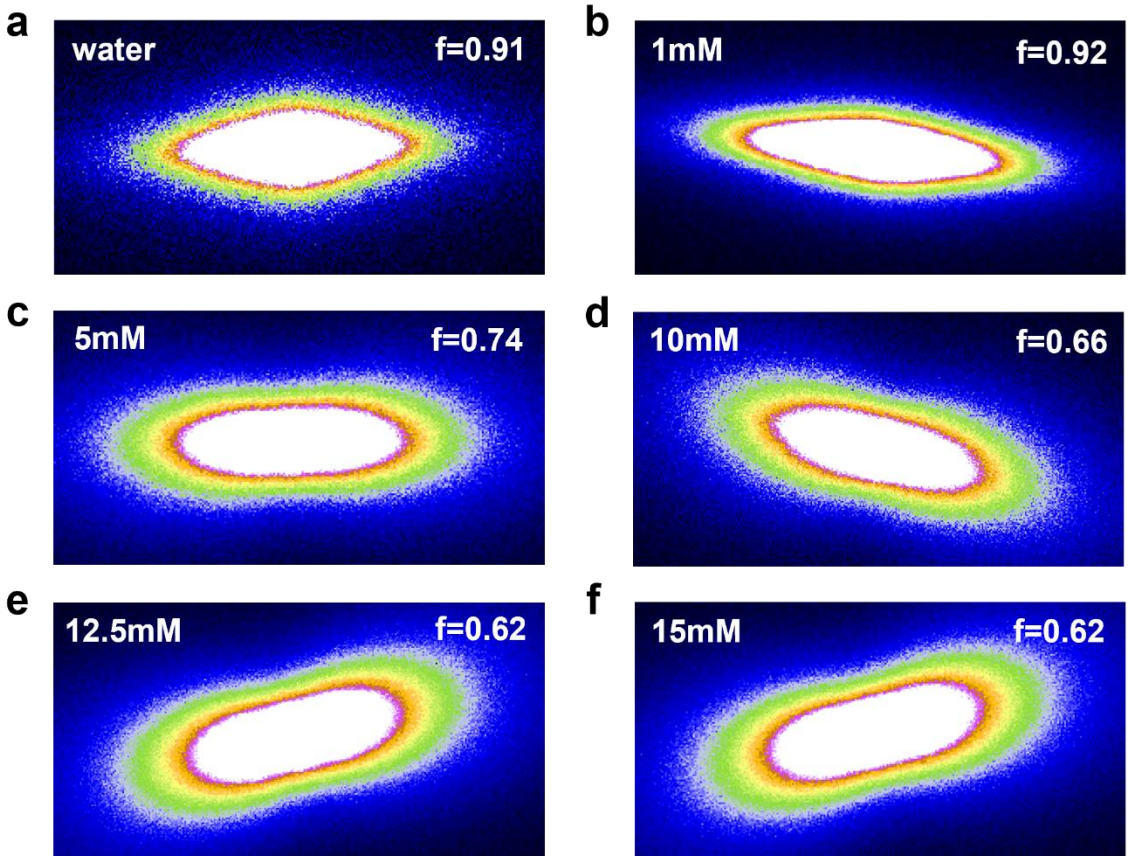


**Fig. S22. SAXS patterns of GO papers with different KCl addition.**

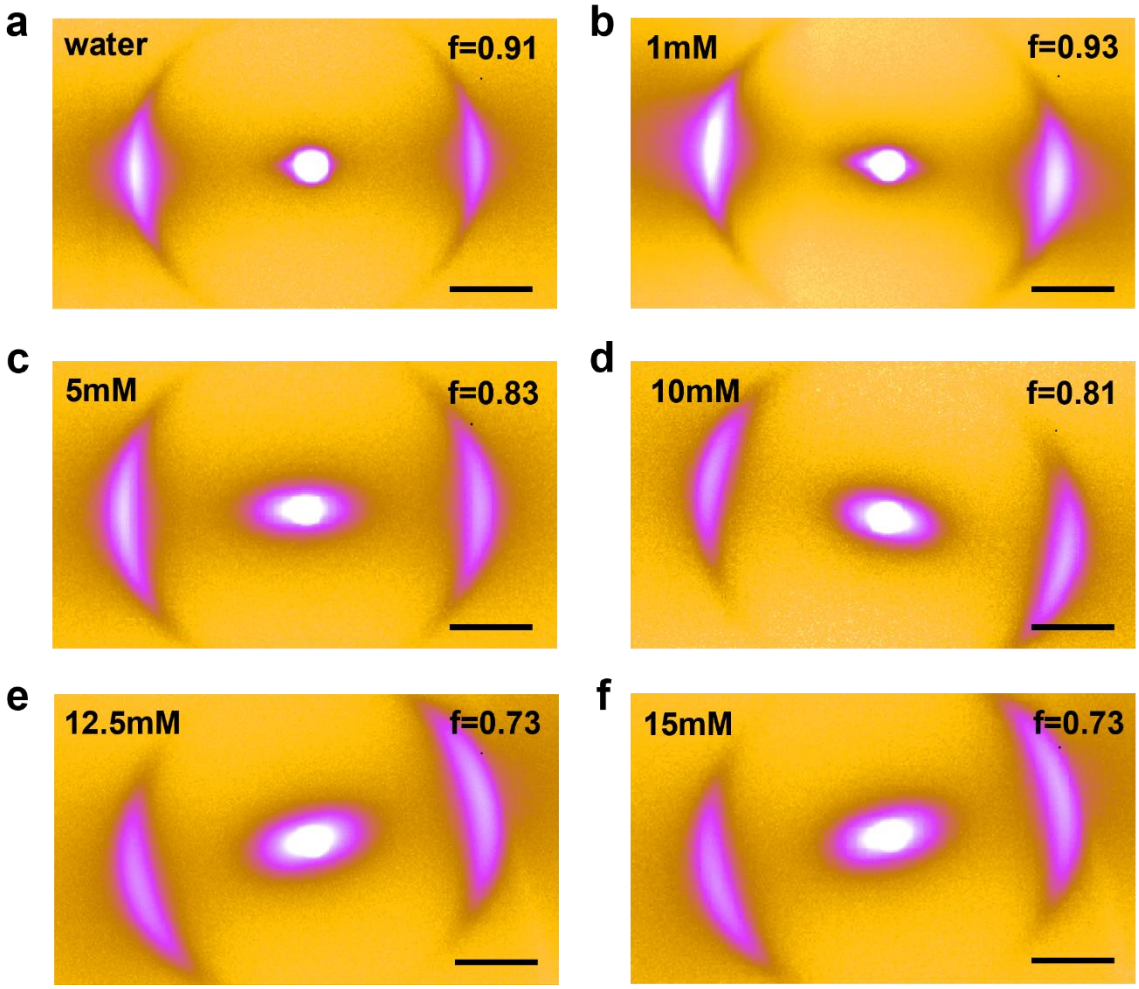


**Fig. S23. WAXS patterns of GO papers with different KCl addition.** Scale bars: 4 $nm^{-1}$.

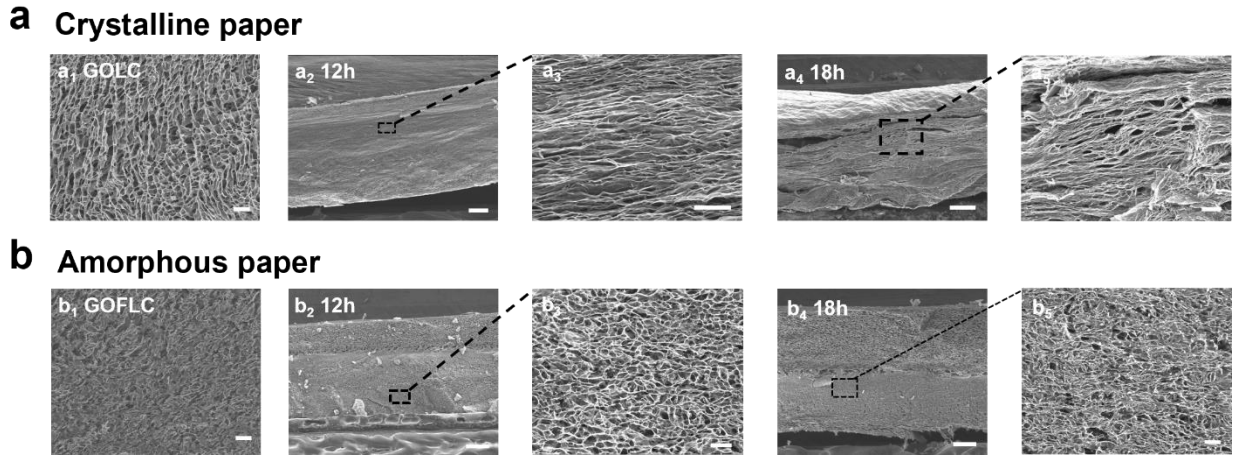


**Fig. S24. The drying process of GO dispersion.** SEM images of the lyophilized GOLC dispersion **(a)** and GOFLC dispersion **(b)** at different drying times. **($a_1$, $b_1$)** t=0 h. **($a_2$, $a_3$, $b_2$, $b_3$)** t=12h. **($a_4$, $a_5$, $b_4$, $b_5$)** t=18h. Scale bars: 40 μm **($a_1$)**; 20 μm **($b_1$)**; 100 μm **($a_2$)**; 250 μm **($b_2$)**; 10 μm **($a_3$)**; 20 μm **($b_3$)**; 50 μm **($a_4$)**; 100 μm **($b_4$)**; 20 μm **($a_5$)**; 10 μm **($b_5$)**.

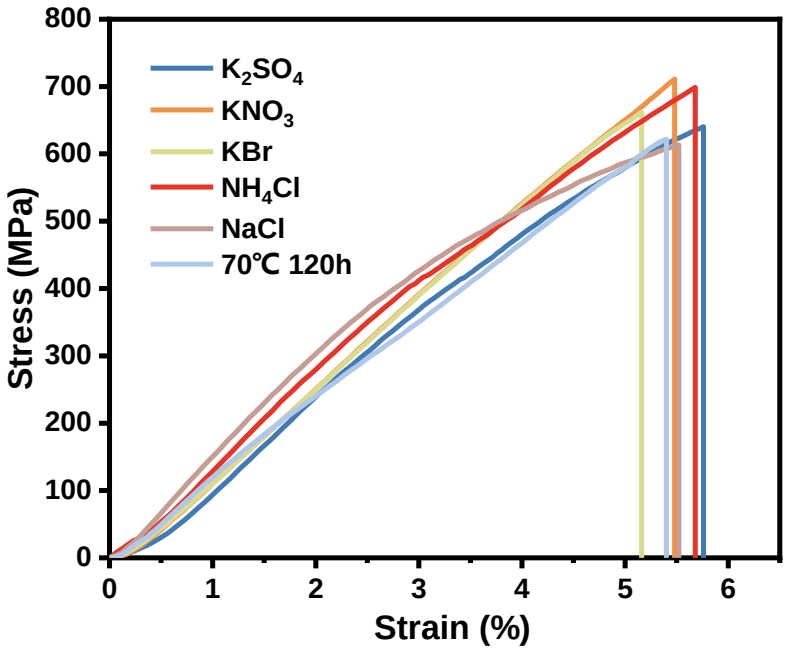


**Fig. S25. Mechanical Properties of reduced GO amorphous papers prepared by the addition of different monovalent salts or moderate heating.**

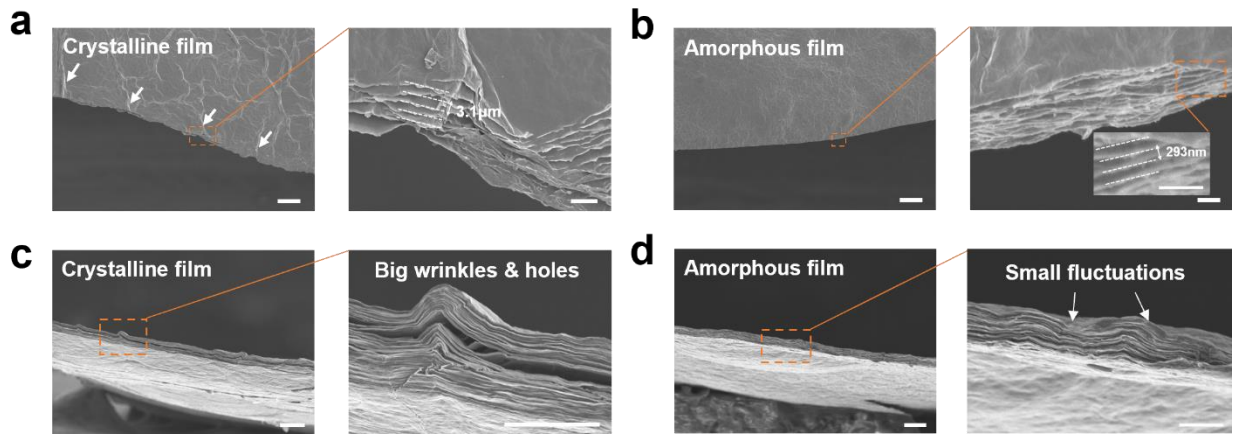


**Fig. S26. The fracture morphologies (a, b) and cross-section SEM images (c, d) of GO crystalline papers and GO amorphous papers.** Scale bars: 40 μm **(a, b**, left**)**; 10 μm **(a**, right**)**; 1 μm **(b**, right**)**; 10 μm **(c, d**, left**)**; 5 μm **(c, d**, right**)**.

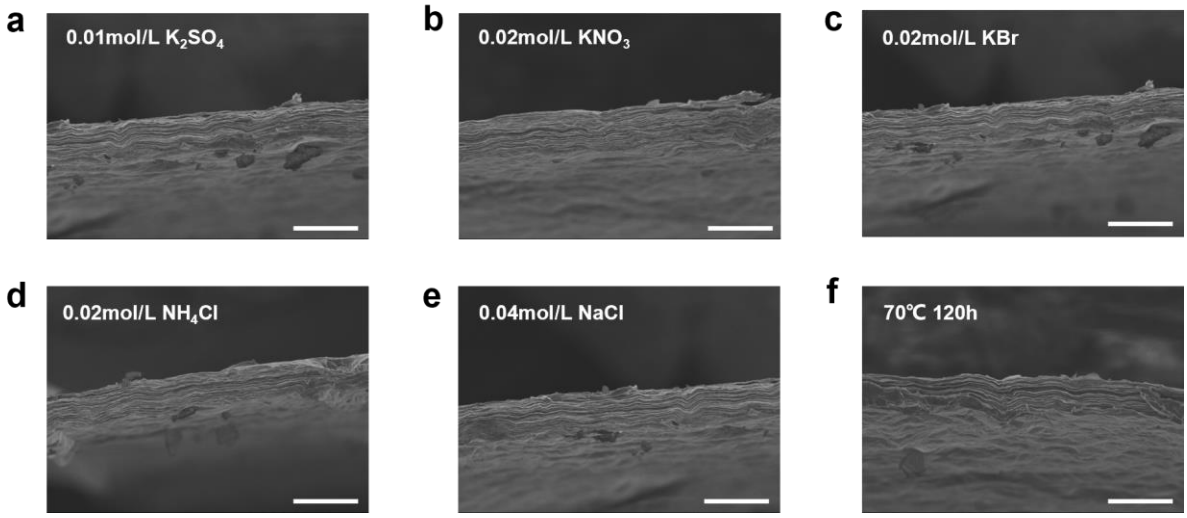


**Fig. S27. Cross-section SEM images of GO amorphous papers assembled from GOFLC dispersions formed by the addition of $K_2SO_4$ (a), $KNO_3$ (b), KBr (c), $NH_4Cl$ (d), NaCl (e) and moderate heating (f).** The concentration of salt in 10mg/g GO is shown on the upper left corner of the picture. Scale bars: 10 μm.

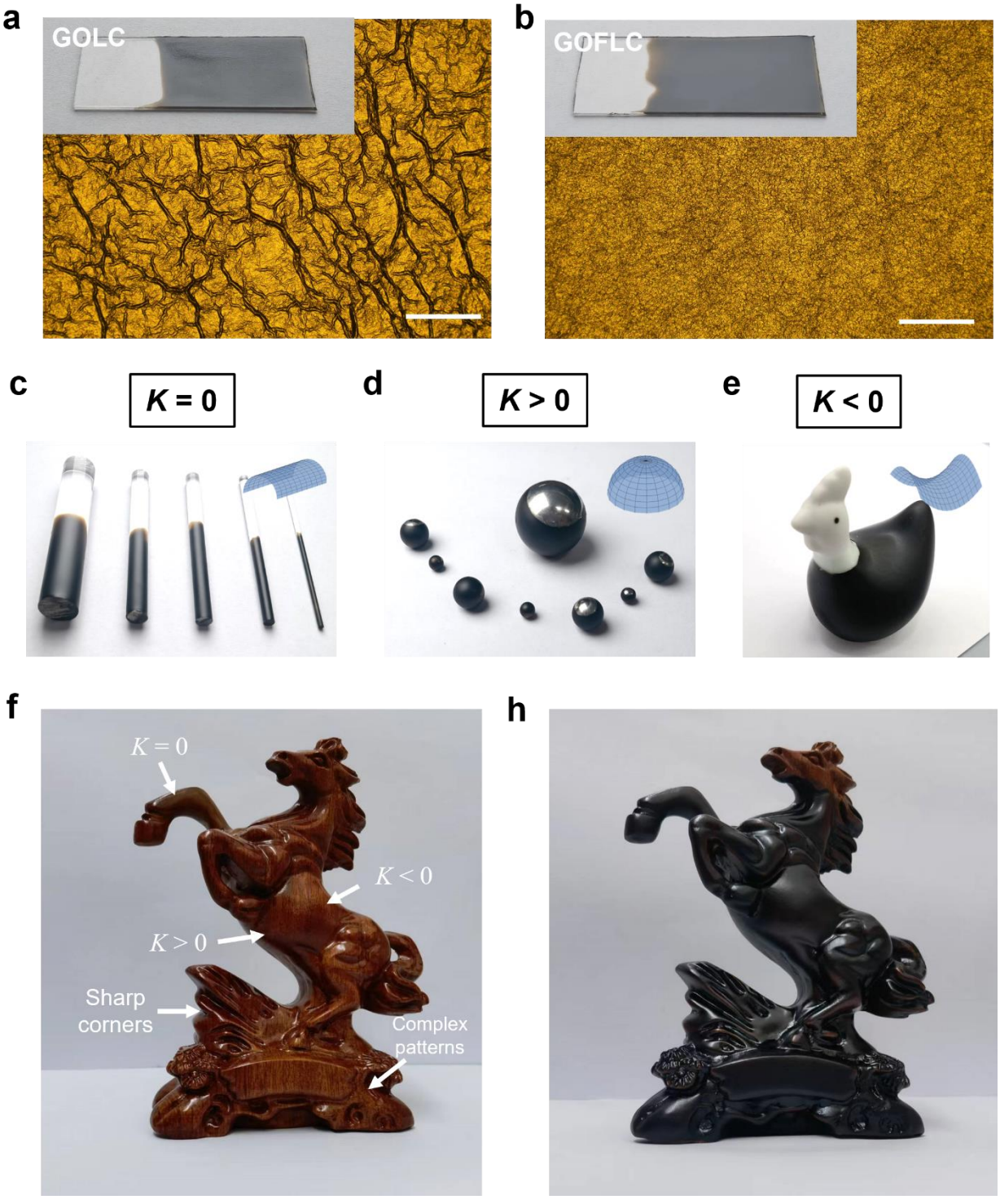


**Fig. S28. Smooth and high-strength GOFLC coatings. a, b** Photographs and OM images of coatings on flat plastic surface made from pure GOLC dispersion **(a)** and GOFLC dispersion **(b)**

**c-e** smooth GOFLC coatings on zero Gaussian curvature surfaces According to the differential geometry, surfaces can be divided into three types based on the Gaussian curvature: zero, positive and negative Gaussian curvature surfaces. Typical representatives of these three surfaces are cylindrical, spherical and saddle surfaces respectively. Therefore, plastic rods, metal balls and ceramic crafts are selected to show the wide applicability of GO FLC coatings on surfaces with different curvatures and materials. **(c)**, positive Gaussian curvature surfaces **(d)** and negative Gaussian curvature surface **(e)**. Inset images are prototype surfaces with different Gaussian curvatures. **(f, g)** smooth GOFLC coatings on complex surfaces. Scale bars: 200 μm **(a, b)**.

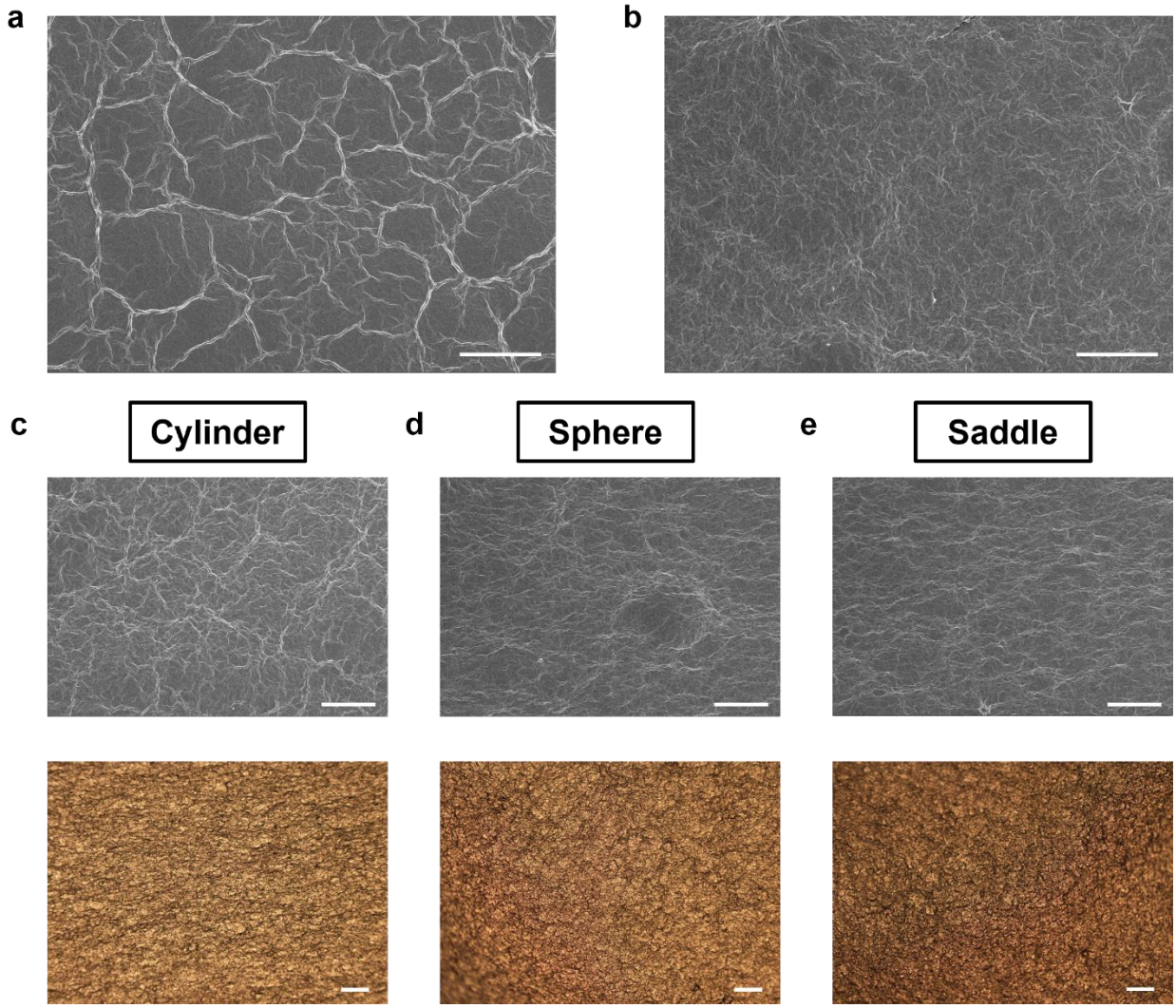


**Fig. S29. The surface morphology of coatings.** SEM images of ordinary GOLC **(a)** and GOFLC **(b)** coatings on flat plastic surface. SEM images and OM images of GOFLC coatings on zero Gaussian curvature cylindrical surfaces **(c)**, positive Gaussian curvature spherical surfaces **(d)** and negative Gaussian curvature saddle surfaces **(e)**. Scale bars: 100 μm.

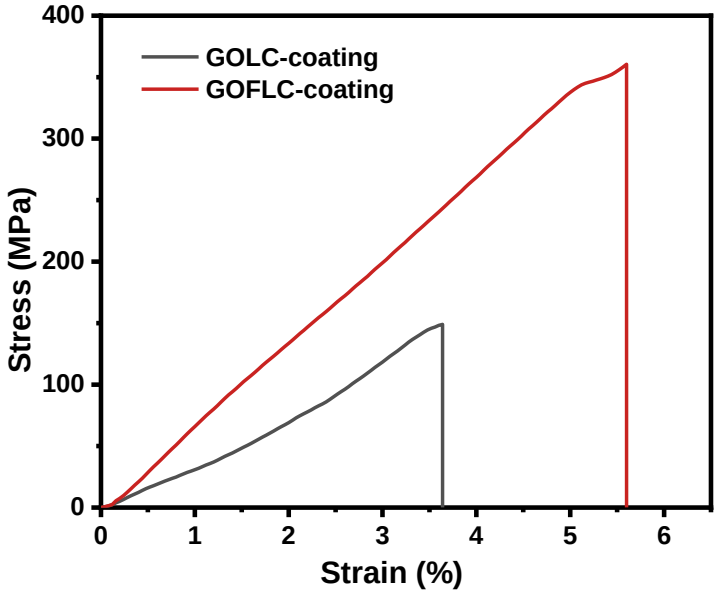


**Fig. S30. Comparison of the mechanical properties of two different coatings.**

## 2. Table S1

| Reference | Strength (MPa) | Young's Modulus (GPa) | Failure Strain (%) | Toughness ($MJ \cdot m^{-3}$) | Preparation | Additive interlayer interaction |
|---|---|---|---|---|---|---|
| Direct cast rGO crystalline paper | 224.7 | 5.98 | 3.76 | 4.22 | Cast; Nematic liquid crystals of graphene oxide | No |
| GOFLC amorphous rGO paper | 747.4 | 13.2 | 5.68 | 21.2 | Cast; Fragmented liquid crystals of graphene oxide | No |
| (51) | 100 | 32 | 0.44 | 0.22 | Vacuum-assisted filtration | No |
| (52) | 129.6 | 1.96 | 7.9 | 3.91 | Vacuum-assited filtration | PCDO crosslinking |
| (53) | 178.9 | 84.84 | 0.2 | 0.179 | Vacuum-assited filtration | PEI crosslinking |
| (54) | 300 | 42.3 | 0.8 | 1.2 | Vacuum-assisted filtration | No |
| (55) | 660 | 20 | 3.1 | ~9.8 | Centrifugal spraying | No |
| (56) | 606 | 43.1 | 1.75 | 5.81 | Vacuum-assisted filtration; GO prepared by modified Hofmann method | No |
| (57) | 1215 | 198.8 | 0.8 | ~4.86 | Superspreading shear-flow-induced alignment | ionic crosslinking |
| (17) | 1100 | 60.27 | 1.6 | 8.25 | Cast; Continuous intercalation modulated plasticization stretching | No |
| (43) | 448 | 51 | 1.28 | 2.4 | Vacuum-assisted filtration; Modified GO with trace carboxyl | No |
| (44) | 774 | 2.5 | 3 | ~10.4 | Layer-by-layer spray coating | No |

| | | | | | | |
|---|---|---|---|---|---|---|
| **(58)** | **944** | **15.134** | **5.6** | **20.6** | **Vacuum-assisted filtration** | **π-π and covalent crosslinking** |
| **(59)** | **1547** | **64.5** | **3.6** | **35.9** | **Vacuum-assited filtration & After-stretching** | **π-π and covalent crosslinking** |
| **(60)** | **1500** | **44.1** | **3.4** | **25.5** | **Cast** | **Strong entanglement caused by ultra-high molecular weight PEO** |
| **(61)** | **765** | **12.3** | **6.22** | **15.64** | **Cast** | **CNC; topological design** |

**Table S1. Comparison of the reduced graphene oxide papers prepared by different methods.**

Our strong and tough amorphous papers prepared by GOFLC dispersions make up for the brittleness of high crystalline papers.

## 3. Calculation based on the DLVO theory

The van der Waals attraction potential energy $V_{\mathrm{A}}$ between two colloidal plates can be calculated by

$$V_{\mathrm{A}} = -\frac{A}{12\pi H^2}\,[\mathrm{J/m^2}], \tag{1}$$

where *A* is the Hamaker constant and *H* is the distance between the plates. The Hamaker constant of GO can be found in the reference to be $4.9\times10^{-20}$ J[37].

The calculation of the electrostatic repulsion potential energy $V_{\mathrm{R}}$ is based on the electrical double layer (EDL) theory. According to the Poisson-Boltzmann equation, the change in the repulsion potential energy with respect to the distance x from the surface of a colloidal particle is

$$\frac{\mathrm{d}^2\varphi}{\mathrm{d}x^2} = \frac{zen^b}{\varepsilon}\left(e^{ze\varphi/kT} - e^{-ze\varphi/kT}\right)\,[\mathrm{V/m^2}]. \tag{2}$$

An approximate solution can be obtained by using the Taylor expansion of $e^x$, namely the Debye-Hückel approximation. Eq. 2 can then be simplified to

$$\frac{\mathrm{d}^2\varphi}{\mathrm{d}x^2} = \kappa^2\varphi\,[\mathrm{V/m^2}], \tag{3}$$

where $\kappa$ is defined as

$$\kappa^2 = \frac{2n^b z^2 e^2}{\varepsilon kT}\,[\mathrm{nm^{-1}}]. \tag{4}$$

To solve the potential energy from Eq. 3, we need two boundary conditions. The first condition is that the electric potential is zero far away from the surface. The second condition is that at some point very close to the surface, the electric potential is $\varphi_{\mathrm{d}}$. In colloidal science, this point refers to the outer boundary of the Stern layer and the Stern layer potential $\varphi_{\mathrm{d}}$ is close to the zeta potential.

The distance from this point outward to the measured position is *x*. With $\varphi(0) = \varphi_{\mathrm{d}}$ and $\varphi(\infty) = 0$, the solution of Eq. 3 is

$$\varphi = \varphi_{\mathrm{d}} e^{-\kappa x} \text{ [V]}. \quad (5)$$

From Eq. 5 we can see the physical meaning of $\kappa$. $\kappa^{-1}$ is the distance from the surface where the potential energy decays to the 1/*e* of the initial value. In this way $\kappa^{-1}$ is a measure of the stretch of the double electric layer and is thus referred to as the EDL thickness or the Debye length $\lambda_D$. We can calculate the Debye length easily from Eq. 4. The following approximation can also be used for aqueous solutions at room temperature:

$$\kappa = \sqrt{10Cz^2} \text{ [nm}^{-1}\text{]}, \quad (6)$$

where *C* (mol/L) is the concentration of ions, and *z* is the number of charges each ion has.

When two colloidal plates come together, their EDLs overlap, introducing the same charge in a region where this kind of charge has already been excessive. Work is required for EDL overlap, and a repulsive force is induced. The electrostatic repulsion potential energy can be calculated by the following equation:

$$V_{\mathrm{R}} = 2\varepsilon\kappa\varphi_{\mathrm{d}}^2 e^{-\kappa H} \text{ [J/m}^2\text{]}, \quad (7)$$

where $\varphi_d$ can be obtained from zeta potential measurements (Figure S10). The total potential energy $V_T$ can be obtained by adding up the van der Waals attraction potential energy $V_{\mathrm{A}}$ and the electrostatic repulsion potential energy $V_{\mathrm{R}}$.

The calculation results of potential energy curves in Figure 3a and the important parameters used in the calculation process are listed in the following table.

| | LC | FLC | Coagulation |
|---|---|---|---|
| A (J) | $4.9\times10^{-20}$ | | |
| $V_{\mathrm{A}}=-\frac{A}{12\pi H^2}$ | $V_{\mathrm{A}}=-\frac{1300}{H(nm)^2}\ (\mu J/m^2)$ | | |
| C (mol/L) | 0.0001 | 0.015 | 0.04 |
| $\kappa$ ($nm^{-1}$) | 0.032 | 0.39 | 0.63 |
| $\lambda_D$ (nm) | 31.3 | 2.56 | 1.59 |
| $\varphi_d$ (mV) | -58.6 | -36.0 | -29.2 |
| $\varepsilon$ (F/m) | $6.95\times10^{-10}$ (water) | | |
| $V_{\mathrm{R}}=2\varepsilon\kappa\varphi_{\mathrm{d}}^2e^{-\kappa H}$ $(\mu J/m^2)$ | $V_{\mathrm{R}}=153e^{-0.032H(nm)}$ | $V_{\mathrm{R}}=703e^{-0.39H(nm)}$ | $V_{\mathrm{R}}=747e^{-0.63H(nm)}$ |
| $V_T=V_{\mathrm{A}}+V_{\mathrm{R}}$ $(\mu J/m^2)$ | $V_T=-\frac{1300}{H(nm)^2}+153e^{-0.032H(nm)}$ | $V_T=-\frac{1300}{H(nm)^2}+703e^{-0.39H(nm)}$ | $V_T=-\frac{1300}{H(nm)^2}+747e^{-0.63H(nm)}$ |

**Table S2. The calculation results of potential energy curves in Figure 3a and the important parameters used in the calculation process**

## 4. CG-MD simulation of fragmented GO LCs

We simulated the effect of different electrostatic repulsion potentials on graphene oxide (GO) LCs using the well-developed CG-MD LC model implemented in LAMMPS[32, 67-69]. Specifically, we applied the Gay-Berne (GB) potential to characterize the interactions between GO particles. The GB potential is a potential function for modeling anisotropic molecular interactions, which is commonly used to model LC molecules, ellipsoids, and other non-spherical particles. Compared with the traditional Lennard-Jones potential, the GB potential considers the orientation and shape of the particles, which can more accurately describe the interaction and orientation dependence of anisotropic molecules, and is helpful for the study of the phase transition and structural behavior of LCs. The most general form of the GB potential ($U_{\mathrm{GB}}$) for non-spherical particles can be expressed as[32, 67, 70]

$$U_{\mathrm{GB}} = 4\epsilon\left[\left(\frac{\sigma}{h_{12}+\gamma\sigma}\right)^{12} - \left(\frac{\sigma}{h_{12}+\gamma\sigma}\right)^{6}\right] \times \eta \times \chi, \qquad (8)$$

where $\epsilon$ and $\sigma$ are the energy scale and particle interaction radius, respectively. $\gamma$ is the shift of the potential minimum. $h_{12}$ is the closest distance between particle surfaces, which is determined by particle size and orientation. The dimensionless quantities $\eta$ and $\chi$ are the shape anisotropy and energy anisotropy parameters, respectively, which depend on the particle dimensions, orientation, and relative well-depth values (i.e., $\epsilon_{ia}$, $\epsilon_{ib}$, $\epsilon_{ic}$, $\epsilon_{ja}$, $\epsilon_{jb}$, and $\epsilon_{jc}$). The relative well depth values define the side-to-side, face-to-face, and end-to-end interactions, with the letters $i$ and $j$ referring to the different interacting particles, and $a$, $b$, and $c$ denoting the direction and size of the semi-axis to which these quantities refer. Noted that, in our simulation, $\epsilon_{ia} = \epsilon_{ja} = \sigma \cdot a/(b \cdot c)$, $\epsilon_{ib} =$

$\epsilon_{jb} = \sigma \cdot b/(a \cdot c)$, and $\epsilon_{ic} = \epsilon_{jc} = \sigma \cdot c/(a \cdot b)$. In LAMMPS, the other two parameters $\upsilon$ and $\mu$ involved in defining $\eta$ and $\chi$ are taken to be 1[67].

In our CG-MD model, as shown in Figure S31A, we utilize ellipsoidal particles to represent GO sheets in the experiment. We considered 4,000 ellipsoidal particles with a thickness of 1 nm, where particles with diameters of 15 μm (largest diameter), 12 μm, 9 μm, and 6 μm (smallest diameter) accounted for 40%, 20%, 20%, and 20% of the total number of particles, respectively. The different particle diameters are intended to describe the anisotropy and shape diversity of the actual GO LC molecules. Specifically, we analyze the evolution of the electrostatic repulsive potential energy between charged 2D colloids with respect to the colloid spacing at different ion concentrations based on the DLVO theory (Figure 3a). The surface repulsion energy densities ($V_R$) between the colloids at ion concentrations of 0.1 mM, 15 mM, and 40 mM are 11.83 μJ/m$^2$, 1.98 × 10$^{-11}$ μJ/m$^2$, and 9.66 × 10$^{-20}$ μJ/m$^2$, respectively. Note that the equilibrium spacing between colloids is typically estimated to be 80 nm. In CG-MD simulations, we fitted the parameters of the GB potential based on the electrostatic repulsion potential-spacing curves of the colloids (Figure 3a), which are utilized to model the effect of $V_R$ on the morphology of GO LCs. The GB potential energy curves and parameters obtained from the fitting are shown in Figure S31B and Table S3, respectively.

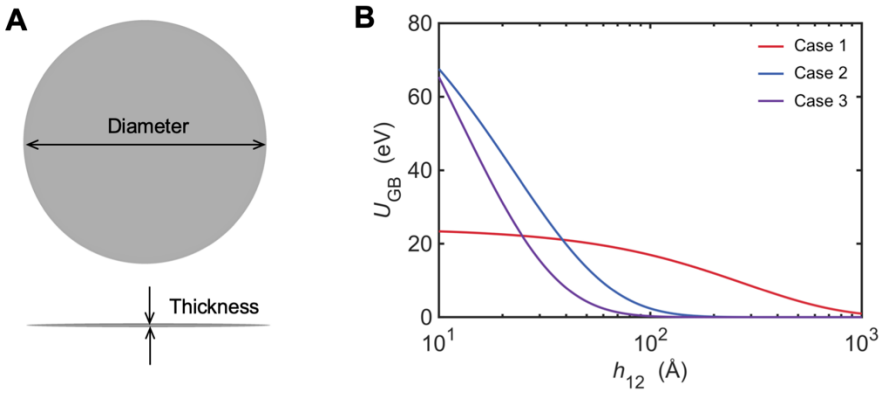


**Fig. S31. (A) Plane and side view of ellipsoidal GO particles. (B) Three GB potentials considered in the CG-MD simulation.**

| GB parameter | Case 1 | Case 2 | Case 3 |
|---|---|---|---|
| Ion concentration | **0.1 mM** | **15 mM** | **40 mM** |
| $V_R$ | **11.83 μJ/m²** | **$1.98 \times 10^{-11}$ μJ/m²** | **$9.66 \times 10^{-20}$ μJ/m²** |
| $\epsilon$ | **$4.031 \times 10^{-3}$ eV** | **$3.108 \times 10^{-8}$ eV** | **$2.382 \times 10^{-8}$ eV** |
| $\sigma$ | **6192** Å | **1493** Å | **854.5** Å |
| $\gamma$ | **0.5424** | **0.1804** | **0.1718** |
| $h_{\text{cutoff}}$ | **3591.7** Å | **1406.5** Å | **812.3** Å |

**Table S3. GB parameters used in the CG-MD simulations.** The parameters are obtained from the fitting of the repulsive potential energy curves calculated from DLVO theory (Figure 3a in the main text). The $\epsilon$ and $\sigma$ for interactions between ellipsoidal particles of different sizes are mixed by arithmetic averaging.

In the CG-MD simulation, all ellipsoidal particles in the initial state are randomly distributed in a cubic simulation box with a side length of 1,000 μm, and the orientation of each particle is random

and the spacing between the centers of every two particles is not less than 15 μm (Figure S32). The temperature and time steps of the simulation are 300 K and 0.05 fs, respectively; the periodic boundary conditions are applied in all directions. The energy of the system is minimized based on an iterative conjugate gradient algorithm[71]. Similar to the work-flow used in previous simulations of the compression behavior of kaolinite based on the GB potential[70], the equilibrium simulations with a duration of 4 ns in both the NVT and NVE ensembles are performed sequentially in our simulations to ensure that the total potential energy of the system converges to an approximately constant value. Then, the system is pressurized from 1 atm to 2,000 atm in 10 ns at NPT ensemble (300 K constant temperature) in all three directions; followed by a further relaxation of 10 ns at 2,000 atm until the compressed system is fully equilibrated. Finally, we quantified the orientation of each particle in the system in the *x*-*z* plane and the degree of LC fragmentation. All of the CG-MD simulations in our study are conducted with the open-source package LAMMPS[72], and the visualization of the CG-MD simulations is realized by OVITO[73].

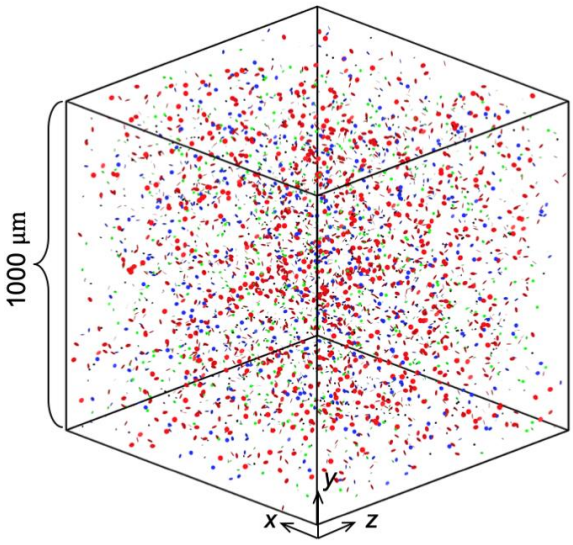

**Fig. S32. Initial CG-MD model in which ellipsoidal particles are spatially and orientationally randomized.** Particles in the snapshot are color-coded according to their size.

The nematic order parameter *f* is a classical metric for quantifying the order and disorder of liquid crystals. For a disordered LC system (i.e., with a high degree of fragmentation), the value of *f* will be closer to 0; while for an ordered LC system, the value of *f* will be closer to 1. Specifically, *f* can be calculated by the following equation[35, 36]

$$f = \frac{1}{2}\langle 3\cos^2\theta - 1\rangle, \quad (9)$$

where $\theta$ is the angle between the GO particle and the selected reference orientation. Here, the reference orientation is the average orientation of all GO particles in the system.

## 5. Discussion on the differences between CG-MD simulation and experiments

The difference in the parameter *f* of GO LCs in simulations and experiments can be explained as follows. First, the periodic boundary conditions and pressurization in simulations limit the free motion of GO sheets and promote orderly stacking of the sheets in a finite space, making *f* larger. In addition, the size and number of GOs in the simulation could not be perfectly matched with that in the experiment due to the limitation of computational resources. The domain size of GO at the same $V_R$ = $1.98\times10^{-11}$ μJ/m$^2$ in the simulation and experiment is about 50 μm and 20 μm, respectively. It is worth noting that the size of the largest GO sheet in the simulation is consistent with the average sheet size of the experimental GO sheet to mimic the real GO LCs system as much as possible. Besides, the simulation simplifies the solvent effect, and the GB potential adopted ignores the van der Waals attraction. In the simulation, the minimum distances of neighboring sheets at $V_R$ = 11.83 μJ/m$^2$, $V_R$ = $1.98\times10^{-11}$ μJ/m$^2$, and $V_R$ = $9.66\times10^{-20}$ μJ/m$^2$ are about 134 nm, 96 nm, and 89 nm, respectively, and the sheets are mainly subject to electrostatic repulsion at this distance in the DLVO theory (Figure 3a).

## 6. Microstructure-aware theory

Microstructure-aware theories, such as the shear-lag model and the deformable tension-shear (DTS) model, can explain the impact of microstructural complexity on the mechanical properties of macroscopic assemblies of GO, including morphological crumples, polydispersity, and intra-layer and inter-layer interactions[62]. In this study, the DTS model is used to analyze the mechanical responses of GOLC and GOFLC papers, which are composed of multiple crumpled basic structural units (BSUs, or closely-packed laminates), as illustrated in Figure 5d in the main text.

The BSUs are staggered layer-by-layer and are interfaced by shear zones between neighboring layers and/or crosslinks in the same layer. For simplification but still in consistency with the experimental evidence, the crumpled profile of the BSUs is treated as a sinusoidal form, $y = a\cos(2\pi x/\lambda)$, where $a$ and $\lambda$ are the respective amplitude and wavelength, and $x$ and $y$ are the coordinates of the BSUs along the in-plane and normal directions. The contour length $l_\mathrm{s}$ of the BSU is $l_\mathrm{s} \approx \int_0^\lambda \left\{1 + \frac{1}{2}\left[\frac{2\pi a}{\lambda}\cos\left(\frac{2\pi x}{\lambda}\right)\right]^2\right\}\mathrm{d}x = \lambda\left[1 + \left(\frac{\pi a}{\lambda}\right)^2\right]$ in a period of crumple. The effective contact size $l_\mathrm{c}$ between two crumpled BSUs can be defined as[49]

$$l_\mathrm{c} = \begin{cases} \dfrac{\lambda}{l_\mathrm{s}} l & \text{for} \quad \omega h_0 \geq 2a \\ \dfrac{\lambda}{l_\mathrm{s}} \dfrac{\arccos\left(1 - \dfrac{\omega h_0}{a}\right)}{\pi} l & \text{for} \quad \omega h_0 < 2a \end{cases}, \tag{10}$$

where $l$ and $h_0$ are the length and thickness of the BSUs, respectively. $\omega > 0$ is a control parameter. The interaction between layers is considered to be lost as the distance between material points in two neighboring BSUs exceeds a critical value of $(1 + \omega)h_0$.

For BSUs in Figure 5d, the equation of mechanical equilibrium is $D\frac{\partial^2 u(x)}{\partial x^2} = 2G\gamma(x)$, where $D = Yh_0$ ($Y$ is Young's modulus) and $G$ are the in-plane tensile stiffness of the BSUs and their interfacial shear modulus, respectively. $u(x)$ and $\gamma(x)$ represent the displacement field in the BSUs along the *x* direction and interlayer shear strain. Eq. 10 can be solved for the interior force $F(x)$ and shear strain $\gamma(x)$ by introducing two boundary conditions, $\frac{\partial u_1(0)}{\partial x} = k\Delta$ and $D\frac{\partial u_2(0)}{\partial x} = F_0$, that are

$$F(x) = \frac{F_0}{2}\left[\frac{1+2\alpha}{1+\alpha} + \frac{1}{1+\alpha}\frac{1+c}{s}\sinh\left(\frac{x}{l_0}\right) - \frac{1}{1+\alpha}\cosh\left(\frac{x}{l_0}\right)\right], \tag{11}$$

$$\gamma(x) = \frac{F_0 l_0}{Dh_0}\left[\frac{1}{1+\alpha}\frac{1+c}{s}\cosh\left(\frac{x}{l_0}\right) - \frac{1}{1+\alpha}\sinh\left(\frac{x}{l_0}\right)\right], \tag{12}$$

where $l_0 = \sqrt{(Dh_0/4G)}$ is the characteristic length of contact required for effective load transfer between adjacent BSUs through shear. $s = \sinh(l_c/l_0)$, $c = \cosh(l_c/l_0)$, $\alpha = 2k_e(1+c)/s$. $F_0$ denotes the bare interior force originating from the elasticity of BSUs. The interaction $F_k$ between BSUs in the same layer is modeled by a linear spring with an elasticity constant of $k$, and the length change of the spring in tension is written as $\Delta$. $k_e = kl_0/D$ is the normalized stiffness of in-plane crosslinks. The in-plane displacements in a pair of contacting BSUs are represented as $u_1(x)$ and $u_2(x)$.

The tensile stress and strain of the system can be expressed as $\sigma_{\mathrm{BSUs}} = (F_0 + F_k)/(2h_0) = F_0(1+2\alpha)/[2h_0(1+\alpha)]$ and $\varepsilon_{\mathrm{BSUs}} = [u_1(l_c) - u_2(0)]/l_c$, respectively. The effective Young's modulus $Y_{\mathrm{eff}}$ of the system can be determined from $Y_{\mathrm{eff}} = \sigma_{\mathrm{BSUs}}/\varepsilon_{\mathrm{BSUs}}$ as

$$Y_{\mathrm{eff}} = \frac{D}{2h_0}\Big/\left(\frac{1}{2} + \frac{1}{1+2\alpha}\frac{1+c}{s}\frac{l_0}{l_c}\right) \tag{13}$$

The system fails by activating sliding between the BSUs as the shear strain exceeds the critical shear strain $\gamma_{\mathrm{cr}}$. The effective tensile strength of the system, $\sigma_{\mathrm{s}} = (F_0 + F_{\mathrm{k}})/(2h_0)$, is thus

$$\sigma_{\mathrm{s}} = \frac{s\gamma_{\mathrm{cr}} D(1+2\alpha)}{2(1+c)l_0}. \tag{14}$$

The toughness $T$ of the system can be estimated based on the area under the stress-strain curve as

$$T = \frac{{\sigma_{\mathrm{s}}}^2}{2Y_{\mathrm{eff}}}. \tag{15}$$

The details of constructing microstructure-aware theories are presented in our previous work[49].

## References

67. R. Everaers, M. R. Ejtehadi, Interaction potentials for soft and hard ellipsoids. *Phys. Rev. E* **67**, 041710 (2003).

68. R. Berardi, C. Fava, C. Zannoni, A Gay-Berne potential for dissimilar biaxial particles. *Chem. Phys. Lett.* **297**, 8-14 (1998).

69. M. P. Allen, G. Germano, Expressions for forces and torques in molecular simulations using rigid bodies. *Mol. Phys.* **104**, 3225-3235 (2006).

70. S. Bandera, C. O'Sullivan, P. Tangney, S. Angioletti-Uberti, Coarse-grained molecular dynamics simulations of clay compression. *Comput. Geotech.* **138**, 104333 (2021).

71. M. C. Payne, M. P. Teter, D. C. Allan, T. A. Arias, J. D. Joannopoulos, Iterative minimization techniques for ab initio total-energy calculations: Molecular dynamics and conjugate gradients. *Rev. Mod. Phys.* **64**, 1045-1097 (1992).

72. S. Plimpton, Fast parallel algorithms for short-range molecular dynamics. *J. Comput. Phys.* **117**, 1-19 (1995).

73. A. Stukowski, Visualization and analysis of atomistic simulation data with OVITO-the Open Visualization Tool. *Modell. Simul. Mater. Sci. Eng.* **18**, 015012 (2010).